Article

Not peer-reviewed version

Perfect Crossed Andreev Reflection in the Staggered Graphene/Superconductor/Periodic Line Defect Superlattice Junctions

Chongdan Ren *, Sake Wang, Minglei Sun, Hongyu Tian *

Posted Date: 16 October 2024

doi: 10.20944/preprints202410.1239.v1

Keywords: crossed Andreev reflection; periodic line defect superlattice; elastic cotunneling doi:10.20944/preprints202410.1239.v1

Article

Perfect Crossed Andreev Reflection in the Staggered Graphene/Superconductor/Periodic Line Defect Superlattice Junctions

Chongdan Ren [1]*, Sake Wang [2], Minglei Sun[3] and Hongyu Tian[4]*

[1] Département de physique, Université normale de Zunyi, Kweichow 563002, China
[2] College of Science, Jinling Institute of Technology, Nanjing 211169, China
[3] NANOlab Center of Excellence, Department of Physics, University of Antwerp, Groenenborgerlaan 171, 2020 Antwerp, Belgium
[4] School of Physics and Electronic Engineering, Linyi University, Linyi 276005, China
* Correspondence: renchongdan@hotmail.com; tianhongyu@lyu.edu.cn

Abstract: We study the crossed Andreev reflection and the nonlocal transport in the staggered graphene/superconductor/periodic line defect superlattice (LDGSL) junctions. The staggered pseudospin potential in the left graphene electrode suppress the local Andreev reflection, while the elastic cotunneling of K′ valley electrons is inhibited due to the exclusive rightward motion of K valley electrons in the right LDGSL electrode, thereby enabling the realization of perfect intravalley crossed Andreev reflection for incident electrons from the K′ valley. Meanwhile, the intravalley elastic cotunneling occurs while both local Andreev reflection and crossed Andreev reflection are completely eliminated for incident electrons in the K valley. Furthermore, the probability of intervalley crossed Andreev reflection scattering is significantly lower than that of intravalley CAR scattering across a broad range of incident angles and electron energies. Our results are helpful for designing the flexible and high-efficiency Cooper pair splitter based on the valley degree of freedom.

Keywords: crossed Andreev reflection; periodic line defect superlattice; elastic cotunneling

1. Introduction

Quantum entanglement among microscopic particles has garnered significant attention due to its intrinsic importance and prospective applications in quantum information technologies[1]. Superconductors are considered natural sources of entangled electrons, as Cooper pairs consist of two electrons with interdependent spin and momentum characteristics[2–9]. Through the process of Cooper pair splitting, spatially separated spin-entangled electrons can be generated at the junction of a conductor and a superconductor. This mechanism's time-reversed counterpart is known as crossed Andreev reflection (CAR) or non-local Andreev reflection. CAR represents a nonlocal process that converts an incoming electron from a voltage-biased lead into an outgoing hole in a spatially separated grounded lead via Cooper pair formation within the grounded superconductor[10,11]. The efficiency of CAR serves as a direct indicator of the effectiveness of Cooper pair splitting.

The realization of the CAR has garnered significant attention in both theoretical and experimental researchers[12–21,21–25]. However, the emergence of CAR is generally accompanied by local Andreev reflection (LAR), normal reflection (NR), and elastic cotunneling (ECT) processes. The LAR process converts an incoming electron from one electrode into a hole within the same electrode, while ECT (or NR) does not involve Cooper pairs and directly transfers or reflects the incoming electron between electrodes. Consequently, CAR can be obscured by the competing processes of ECT and LAR, leading to a complete cancellation of the conductivities associated with ECT and CAR. This necessitates the use of noise measurements to identify the distinct signature of the CAR process within superconducting heterostructures.

Recent advancements have proposed methods to enhance CAR signals by mitigating both ECT and LAR processes through various types of leads, including normal metals, ferromagnetic metals, antiferromagnetic metals, and topological insulators[26–34]. For instance, perfect CAR has been achieved in hybrid junctions formed by n-type and p-type semiconductors through band-structure-induced energy filtering[6]. Specialized circuits utilizing helical edge states of topological insulators have been designed to achieve perfect CAR[27]. Additionally, a robust signature of perfect CAR has been observed in superconductors situated between two antiferromagnetic layers, with one being electron-doped and the other hole-doped[32].

Furthermore, CAR can be realized in graphene/superconductor/graphene junctions by exploiting the valley degree of freedom[35–40]. Initial investigations into graphene-based devices aimed to achieve perfect CAR primarily focused on the zero density of states at the Dirac point[35]. In a zigzag graphene nanoribbon/superconductor/nanoribbon junction, exclusive CAR can be attained with complete suppression of both ECT and LAR, attributable to the valley selection rule in even zigzag nanoribbons[37]. The introduction of a staggered pseudospin potential and intrinsic spin-orbit coupling within graphene enables perfect CAR for electrons with a designated spin-valley index[40].

In this study, we propose a distinct mechanism to achieve valley-dependent perfect CAR in proximitized graphene/superconductor/periodic line defect superlattice (LDGSL) junctions. The lattice structure of the LDGSL, characterized by periodically embedded extended line defects along the y-direction[41], is illustrated in Figure 1(a). The dispersion of the LDGSL at $k_y = 0$ is depicted in Figure 1(c). Notably, the lowest conduction band of the LDGSL exhibits a valley-dependent electron velocity direction, permitting rightward motion in the K valley and leftward motion in the K$'$ valley. This band structure allows the LDGSL to function as a valley filter. In our junction configuration, the left graphene electrode features a pseudospin staggered potential induced by the proximity effect of the substrate[42–47]. We first demonstrate that if the left graphene electrode is gapless, LAR diminishes the occurrence of CAR. Upon introducing the staggered pseudospin potential, the left graphene electrode becomes insulating for the hole band, enabling perfect CAR for K$'$ electrons while completely suppressing LAR and ECT. Conversely, ECT can manifest for K electrons while both LAR and CAR are suppressed. Moreover, both CAR and ECT processes are predominantly governed by intra-valley scattering. Additionally, we analyze the relationship between scattering probabilities and the incident angle θ, demonstrating that both inter-valley and intra-valley scattering probabilities rise with increasing θ, while intra-valley scattering probabilities considerably surpass those of inter-valley scattering. This indicates that nearly perfect crossed Andreev reflection (CAR) with incident K$'$ valley electrons can be achieved across a wide range of incident angles and energy.

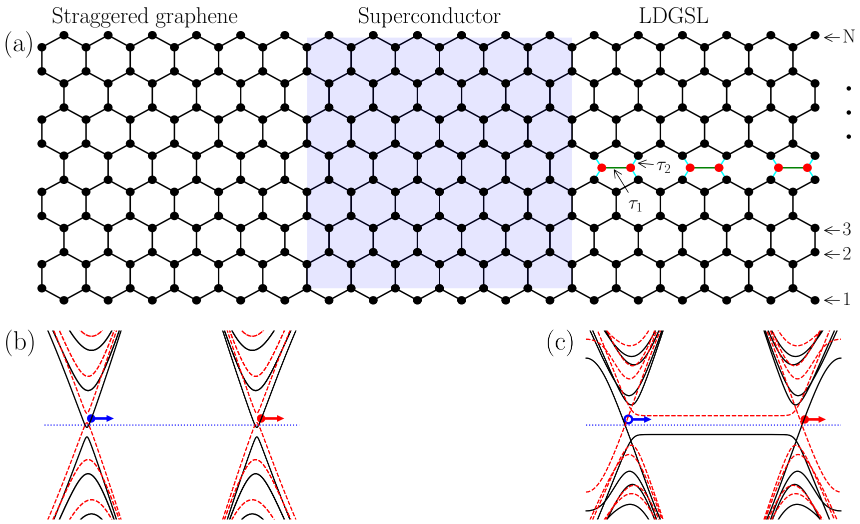

Figure 1. (a) Schematic representation of the proposed proximitized graphene/superconductor/LDGSL junctions. N indicates the transverse dimension of the unit cell of the LDGSL. τ_1 and τ_2 represent the hopping energies associated with the carbon-carbon bonds around the line defect. It is assumed that a bias voltage V is applied to the left graphene electrode, while the superconductor and the right LDGSL are ground. Panels (b) and (c) depict the dispersion relations for electrons (solid black lines) and holes (dashed red lines) in the left proximitized graphene and the right LDGSL, respectively. The solid red circle denotes K electrons, whereas the blue solid (hollow) circles represent K$'$ electrons (holes). The arrows illustrate the direction of motion. The scattering processes for CAR (ECT) of K$'$ (K) electrons, excluding the contributions from LAR and ECT (CAR), are illustrated in panels (b) and (c).

The structure of the remainder of the paper is as follows. Section 2 presents the proposed structure and establishes the theoretical framework for calculating valley-related scattering probabilities as well as local and nonlocal conductances. In Section 3, we provide numerical results regarding intra-valley and inter-valley scattering for the NR, LAR, ECT, and CAR processes, along with the local and nonlocal conductance within the proposed structure. Finally, Section 4 offers a brief summary of the findings.

2. Theoretical Modeling

In Figure 1(a), we present a schematic representation of the proximitized graphene /superconductor/LDGSL configuration within the xy plane, with junction interfaces located at $x = 0$ and $x = L$, where electronic transport is directed along the x-axis. The staggered potential Δ in the left graphene is attributed to the substrate, while the superconducting gap Δ_0 in the central region is induced by a bulk superconductor via the proximity effect. The right section features a one-dimensional LDGSL superlattice, created by periodically embedding extended line defects along the y direction in pristine graphene. The unit cell size of the LDGSL in the x direction measures $2a$ with a being the graphene lattice constant, while the dimension in the y direction is characterized by the integer N[41]. The hopping energies τ_1 and τ_2 between nearest-neighbor lattice points on the line defect within the tight-binding model may differ from the uniform nearest-neighbor hopping energy t of pristine graphene, indicating lattice distortion surrounding the line defect.

The following model Hamiltonian is employed here to describe the system:

$$H = H_L + H_R + H_S \tag{1}$$

where H_L describes the left proximitized graphene with straggered potential, H_S denoted a superconducting graphene caused by a bulk superconductor through proximity effect, and H_R stands for the

doi:10.20944/preprints202410.1239.v1

LDGSL electrode. In the tight-binding representation, the Hamiltonians H_L, H_S and H_R are defined as follows:

$$H_L = -t\sum_{\langle i,j\rangle} c_i^\dagger c_j + \sum_i \Delta\xi_\beta c_i^\dagger c_i - \mu_L \sum_i c_i^\dagger c_i \tag{2}$$

$$H_S = -t\sum_{\langle i,j\rangle} c_i^\dagger c_j + \sum_i \Delta_0\left(c_{i\uparrow}^\dagger c_{i\downarrow}^\dagger + c_{i\downarrow}c_{i\uparrow}\right) - \mu_S \sum_i c_i^\dagger c_i \tag{3}$$

$$H_R = -t\sum_{\langle i,j\rangle} c_i^\dagger c_j - \left[\tau_1 \sum_i d_{i,A}^\dagger d_{i,B} + \tau_2 \sum_{\langle i,\alpha\rangle} c_i^\dagger d_{i,\alpha} + h.c.\right] - \mu_R \sum_i c_i^\dagger c_i \tag{4}$$

where $c_i^\dagger$ and $d_{i,\alpha}^\dagger$ represent the creation operators for an electron at lattice site i and in sublattice α of the line defect, respectively. $\langle ...\rangle$ refer to nearest-neighbor sites. The hopping integral is represented by t, and Δ denotes the on-site staggered potential, where $\xi_A = 1$ corresponds to sublattice A and $\xi_B = -1$ to sublattice B. Δ_0 refers to the induced superconducting pairing. Additionally, $\tau_{1(2)}$ signifies the hopping energy associated with carbon-carbon bonds surrounding the line defect, and $\mu_{L(S,R)}$ represents the Fermi level, which can be modulated through gate voltage technology.

The valley-dependent transmission coefficients are determined utilizing the S-matrix method, a widely recognized approach in the field of mesoscopic physics[48]. In this investigation, we numerically implement the S-matrix method through KWANT[49], a Python library specifically designed for calculating the S-matrix of scattering regions within tight-binding frameworks. The model previously defined is compatible with the KWANT methodology for S-matrix computations. The scattering matrix τ yields the scattering amplitude $\tau_{k_1k_2,\alpha\beta}^{ij}$, which describes the transmission from the incoming k_2 state of particle type β in lead j to the outgoing k_1 state of particle type α in lead i[50]. Subsequently, the valley-dependent transmission coefficients can be derived using the following formula:

$$T_{K_1K_2,\alpha\beta}^{ij} = \sum_{k_1\in K_1}\sum_{k_2\in K_2}\left|\tau_{k_1k_2,\alpha\beta}^{ij}\right|^2 \tag{5}$$

where $T_{K_1K_2,ee}^{LL}$ and $T_{K_1K_2,he}^{LL}$ denote the valley-dependent NR and LAR processes, respectively, while $T_{K_1K_2,ee}^{RL}$ and $T_{K_1K_2,he}^{RL}$ refer to the valley-related ECT and CAR processes. Furthermore, the condition K_1=K_2 signifies intravalley scattering, whereas $K_1 \neq K_2$ indicates intervalley scattering.

Based on the Blonder-Tinkham-Klapwijk framework[51], the valley-dependent normalized conductance matrix at a bias voltage V and at zero temperature can be expressed as follows:

$$\sigma_{K_1}^{ij}(eV) = \frac{e^2}{h} \times \frac{\sum\limits_{k_y}\delta_{ij}N_{K_1,e}^{j} - T_{K_1K_1,ee}^{ij} - T_{K_1K_2,ee}^{ij} + T_{K_1K_1,he}^{ij} + T_{K_1K_2,he}^{ij}}{\sum\limits_{k_y} N_{K_1,e}^{j}(k_y)} \tag{6}$$

where $N_{K_1,e}^{j}$ represents the number of transverse modes associated with the K_1 valley in the left graphene at the transverse wavevector k_y. The terms $\sigma_{K_1}^{ij}$ correspond to the local conductance when $i = j$ and the nonlocal conductance when $i \neq j$. Additionally, k_y serves as a conserved quantum number due to the translational symmetry along the y-axis.

3. Numerical Results

In our calculations, we use the superconducting gap $\Delta_0 = 0.001\,\text{eV}$ as the unit of energy. μ_S is taken as $\mu_S = 20\Delta_0$, ensuring quasiparticle propagation parallel to the x axis. Similarly, μ_R is also set to $20\Delta_0$, ensuring that the energy range under consideration remains within the flat lowest conduction band and the corresponding hole band, thereby excluding minor dips near the K and K′ points from transport. μ_L is designated as $0.5\Delta_0$. Suppose a variation of less than 5% in the hopping terms τ_1 and

τ_2, and here we adopt $\tau_1 \approx \tau_2 \approx t = 2.8\,\text{eV}$[52]. The length of the superconducting region is set to $L = 50a$, while the width of a unit cell of the LDGSL is set to $N = 32$.

Firstly, we consider the left graphene without the pseudospin staggered potential, i.e., $\Delta = 0$, resulting in gapless and linear dispersion for both electrons and holes in graphene. Figure 2 illustrates the intra- and intervalley scattering spectra for NR, LAR, CAR, and ECT processes as a function of incident energy E at $k_y = 0$ (*i.e.*,normal incidence with $\theta = 0$). For the ECT process, only the intra-valley transmission $T^{RL}_{KK,ee}$ is significant, while other processes can be disregarded (see Figure 2(c)). This valley filtering effect arises from the existence of a single rightward propagating mode in the K valley within the right LDGSL electrode. In the case of LAR, both K and K′ related intervalley scattering ($T^{LL}_{K'K,he}$ and $T^{LL}_{KK',he}$) are present within the energy range $0 < E < \Delta_0$. Notably, $T^{LL}_{K'K,he}$ is less than $T^{LL}_{KK',he}$ due to the ability of K valley electrons to tunnel into the right LDGSL electrode, whereas K′ valley electrons can only be normally reflected (see Figure 2(a)). In contrast to LAR and ECT, all intra- and intervalley CAR processes can be neglected, as demonstrated in Figure 2(d). Thus, this configuration employs the right LDGSL electrode to block tunneling of K′ valley electrons. Additionally, for CAR to take place, it is essential to suppress LAR process occurring in the left electrode.

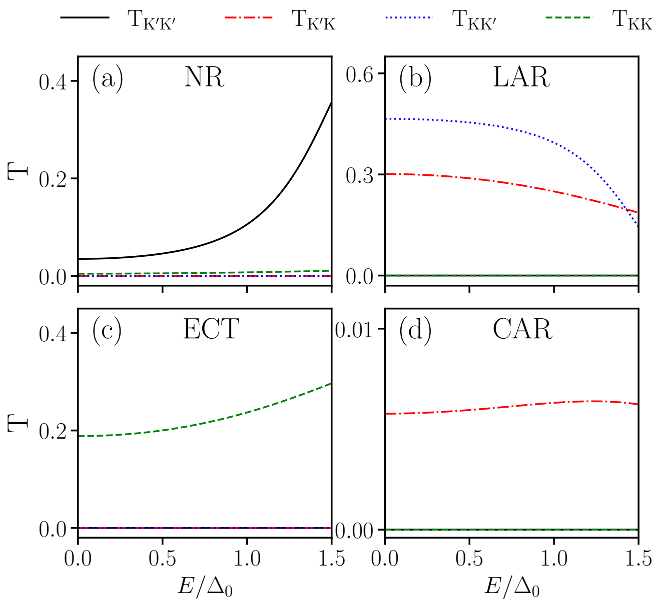

Figure 2. Plots of the transmission probabilities for intra- and intervalley NR (a), LAR (b), ECT (c), and CAR (d) as functions of the incident electronic energy E at an incident angle of $\theta = 0$, specifically for the condition where $\Delta = 0$. $T_{K_1K_2}$ denotes the transmission probability of K_2 valley particles to K_1 valley particles.

The LAR process can be suppressed by utilizing either n-type or p-type graphene, based on the principle that an electron cannot be reflected as a hole within the same electrode when the hole band is artificially made insulating. When a pseudospin staggered potential $\Delta \neq 0$ is introduced, an energy gap of 2Δ emerges. This gap for electrons extends from $-\Delta - \mu_L$ to $\Delta - \mu_L$, while the corresponding gap for holes spans from $-\Delta + \mu_L$ to $\Delta + \mu_L$. Within the energy range defined by the hole band gap, LAR is absent for incident electrons. In Figure 3, we consider the scattering spectra under a finite pseudospin staggered potential of $\Delta = 0.25\Delta_0$, with other parameters consistent with those in Figure 2. As anticipated, LAR is zero within the energy range $0.25\Delta_0 < E < 0.75\Delta_0$ and nonzero outside this interval, as demonstrated in Figure 3(b). Furthermore, nonlocal ECT processes associated with intravalley scattering $T^{RL}_{K'K',ee}$ are prohibited, while those related to intervalley scattering $T^{RL}_{KK',ee}$ are minimal (refer to Figure 3(c)). Consequently, CAR can occur in the injection of K′ electrons $T^{RL}_{K'K',he}$ without LAR and ECT (shown in Figure 3(d)), even outside the superconducting gap, as depicted in the inset of Figure 3(d). In contrast, for incident K electrons within the energy gap of hole gap, both LAR processes ($T^{LL}_{K'K,he}$ and $T^{LL}_{KK,he}$) as well as intra-valley CAR $T^{RL}_{KK,he}$ are zero, while inter-valley CAR $T^{RL}_{K'K,he}$ is negligibly small, leaving only a finite intra-valley ECT $T^{RL}_{KK,ee}$. Thus, by analyzing the carrier type in the right LDGSL electrode, it is possible to ascertain whether the incident electron is a K or K′ valley electron. Furthermore, unlike the previous scenario where $\Delta_0 = 0$, the intervalley NR processes $T^{LL}_{K'K,ee}$ and $T^{LL}_{KK',ee}$ occur alongside $T^{LL}_{K'K',ee}$ from both valleys, as demonstrated in Figure 3(a).

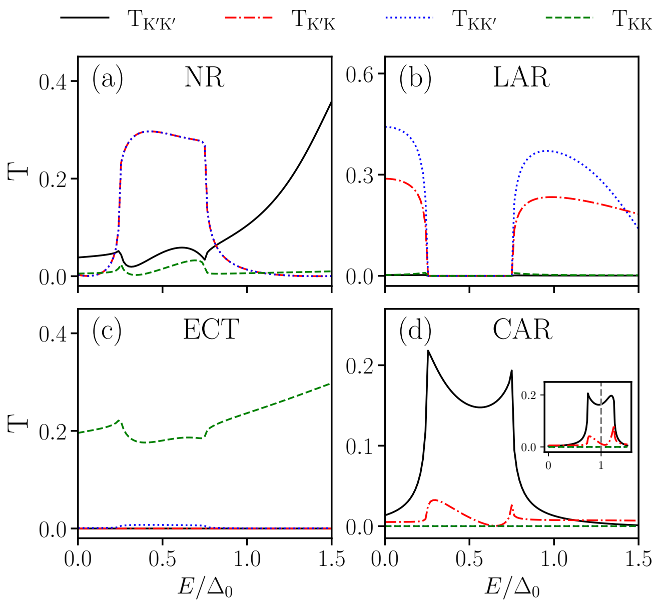

Figure 3. Plots of the transmission probabilities for intra- and intervalley NR (a), LAR (b), ECT (c), and CAR (d) as a function of the incident electronic energy E at an incident angle of $\theta = 0$, under the condition where $\Delta = 0.25\Delta_0$. $T_{K_1K_2}$ denotes the transmission probability of K_2 valley particles to K_1 valley particles. Aside from $\mu_L = \Delta_0$, all other parameters in the inset of panel (d) are consistent with those in panel (d).

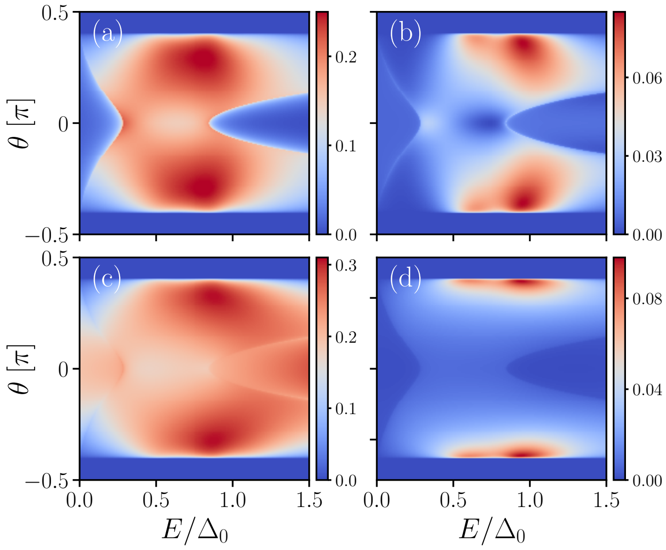

Figure 4. (a) Intra-valley CAR probabilities for incident K' electrons, denoted as $T^{RL}_{K'K',he}$, in the (E,θ) space; (b) Inter-valley CAR probabilities for incident K electrons, represented as $T^{RL}_{K'K,he}$, in the (E,θ) space; (c) Intra-valley ECT probabilities for incident K electrons, denoted as $T^{RL}_{KK,ee}$, in the (E,θ) space; (d) Inter-valley ECT probabilities for incident K' electrons, represented as $T^{RL}_{KK',ee}$, in the (E,θ) space. The parameters are consistent with those presented in Figure (3).

To achieve a more comprehensive understanding of the interplay between CAR and ECT with respect to the angle of incidence, we present the inter- and intra-valley CAR and ECT probabilities within the (E,θ) parameter space. When the energy of the incident electron at the left electrode falls within the energy gap of the corresponding hole and the angle of incidence is near $\theta = 0$, the probabilities for both intra- and inter-valley CAR and ECT exhibit minimal variation, with intra-valley scattering probabilities markedly surpassing those of inter-valley scattering. This phenomenon suggests that when electrons from the K′ valley impinge upon the left electrode, nearly ideal CAR occurs at the right LDGSL electrode, while ECT is observed for electrons originating from the K valley. As the angle of incidence θ increases, the energy ranges favorable for intra-valley CAR and ECT expand, a result attributed to the increasing band gap of the left graphene electrode. Concurrently, both intra-valley and inter-valley scattering probabilities increase with θ. The enhancement of inter-valley CAR and ECT scattering can be attributed to the decreasing energy separation between the two valleys in the band structure of the right LDGSL electrode as θ escalates. The increase in intra-valley scattering with θ can be elucidated by the upward shift of the conduction band minimum in the left graphene, which facilitates a more effective alignment of the conduction band slopes between the two electrodes.

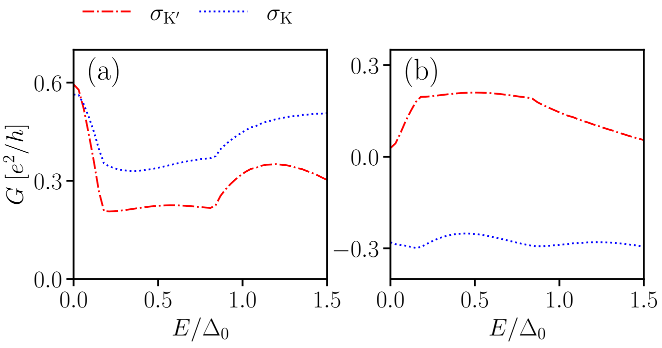

Figure 5. Normalized local (a) and nonlocal (b) conductance spectra for the K and K' electrons.

Finally, We examine both local and nonlocal conductance. The local conductance for incoming electrons from the K and K$'$ valleys exhibits a notable reduction as the bias voltage increases from $V = 0$. Importantly, within the energy interval $0.25\Delta_0 < E < 0.75\Delta_0$, where no holes are present, the local conductance does not converge to zero, as typically observed in two-terminal graphene/superconductor junctions; rather, it indicates the contribution of nonlocal processes. Furthermore, the LAR within the energy range $0 < E < 0.25\Delta_0$ corresponds to retro-Andreev reflection, whereas the LAR within the energy range $0.75\Delta_0 < E < \Delta_0$ is associated with specular Andreev reflection. Regarding nonlocal conductivity, for incident electrons in the K' valley, the conductivity remains relatively constant within the energy gap, facilitating nearly ideal CAR. However, as the energy of the incident electrons deviates from the energy gap, the CAR decreases towards zero. Conversely, for electrons originating from the K valley, the nonlocal conductivity remains largely stable both inside and outside the energy gap. Within the energy gap, the total conductivity is low due to the cancellation between CAR and ECT, while outside the energy gap, it approaches a value determined primarily by ECT.

4. Conclusions

In conclusion, this investigation presents an new approach for achieving valley-dependent perfect CAR in straggered graphene/superconductor/LDGSL junctions. By employing a staggered pseudospin potential and the valley-filtering effect of the LDGSL, we effectively suppress LAR and ECT, thereby facilitating perfect intra-valley CAR. The results indicate that intra-valley CAR scattering is predominantly unaffected by the angle of incidence and is considerably greater than inter-valley CAR scattering. These findings make a important contribution to the understanding of electron transport phenomena in defect-based junctions and highlight the potential for harnessing valley-dependent physics within quantum information technologies.

Author Contributions: C.Ren.: Formal analysis, investigation and writing—original draft preparation; S.Wang.: Formal analysis and validation; M.Sun. : Data curation and validation; H.Tian: Formal analysis; C.Ren.: Conceptualization and writing—review and editing. All authors have read and agreed to the published version of the manuscript.

Funding: This research was funded by the National Natural Science Foundation of China (Grant No. 12264059), the Natural Science Foundation of Shandong Province (Grant No. ZR2019MA030).

Institutional Review Board Statement: Not applicable.

Informed Consent Statement: Not applicable.

Data Availability Statement: The codes generated during the simulation study are available from the corresponding author upon reasonable request.

Conflicts of Interest: All the authors declare that they have no conflict of interest.

References

1. Vidal, G. Efficient classical simulation of slightly entangled quantum computations. *Physical review letters* **2003**, *91*, 147902. doi:10.1103/PhysRevLett.91.147902.
2. Chtchelkatchev, N.M.; Blatter, G.; Lesovik, G.B.; Martin, T. Bell inequalities and entanglement in solid-state devices. *Physical Review B* **2002**, *66*, 161320. doi:10.1103/PhysRevB.66.161320.
3. Sauret, O.; Martin, T.; Feinberg, D. Spin-current noise and Bell inequalities in a realistic superconductor-quantum dot entangler. *Physical Review B* **2005**, *72*, 024544. doi:10.1103/PhysRevB.72.024544.
4. Nilsson, J.; Akhmerov, A.R.; Beenakker, C.W.J. Splitting of a Cooper pair by a pair of Majorana bound states. *Physical review letters* **2008**, *101*, 120403. doi:10.1103/PhysRevLett.101.120403.
5. Hofstetter, L.; Csonka, S.; Nygård, J.; Schönenberger, C. Cooper pair splitter realized in a two-quantum-dot Y-junction. *Nature* **2009**, *461*, 960–963. doi:10.1038/nature08432.
6. Veldhorst, M.; Brinkman, A. Nonlocal Cooper Pair Splitting in a pSn Junction. *Physical Review Letters* **2010**, *105*, 107002. doi:10.1103/PhysRevLett.105.107002.
7. Hofstetter, L.; Csonka, S.; Baumgartner, A.; Fülöp, G.; d'Hollosy, S.; Nygård, J.; Schönenberger, C. Finite-bias Cooper pair splitting. *Physical review letters* **2011**, *107*, 136801. doi:10.1103/PhysRevLett.107.136801.

8. Tan, Z.B.; Cox, D.; Nieminen, T.; Lähteenmäki, P.; Golubev, D.; Lesovik, G.B.; Hakonen, P.J. Cooper pair splitting by means of graphene quantum dots. *Physical review letters* **2015**, *114*, 096602. doi:10.1103/PhysRevLett.114.096602.
9. Pandey, P.; Danneau, R.; Beckmann, D. Ballistic Graphene Cooper Pair Splitter. *Physical review letters* **2021**, *126*, 147701. doi:10.1103/PhysRevLett.126.147701.
10. Recher, P.; Sukhorukov, E.V.; Loss, D. Andreev tunneling, Coulomb blockade, and resonant transport of nonlocal spin-entangled electrons. *Physical Review B* **2001**, *63*, 165314. doi:10.1103/PhysRevB.63.165314.
11. Zhu, Y.; Sun, Q.f.; Lin, T.h. Andreev reflection through a quantum dot coupled with two ferromagnets and a superconductor. *Physical Review B* **2001**, *65*, 024516. doi:10.1103/PhysRevB.65.024516.
12. Yamashita, T.; Takahashi, S.; Maekawa, S. Crossed Andreev reflection in structures consisting of a superconductor with ferromagnetic leads. *Physical Review B* **2003**, *68*, 174504. doi:10.1103/PhysRevB.68.174504.
13. Mélin, R.; Peysson, S. Crossed Andreev reflection at ferromagnetic domain walls. *Physical Review B* **2003**, *68*, 174515. doi:10.1103/PhysRevB.68.174515.
14. Mélin, R.; Feinberg, D. Sign of the crossed conductances at a ferromagnet/superconductor/ferromagnet double interface. *Physical Review B* **2004**, *70*, 174509. doi:10.1103/PhysRevB.70.174509.
15. Beckmann, D.; Weber, H.B.; Löhneysen, H.V. Evidence for crossed Andreev reflection in superconductor-ferromagnet hybrid structures. *Physical review letters* **2004**, *93*, 197003. doi:10.1103/PhysRevLett.93.197003.
16. Benjamin, C. Crossed Andreev reflection as a probe for the pairing symmetry of ferromagnetic superconductors. *Physical Review B* **2006**, *74*, 180503. doi:10.1103/PhysRevB.74.180503.
17. Cadden-Zimansky, P.; Chandrasekhar, V. Nonlocal correlations in normal-metal superconducting systems. *Physical review letters* **2006**, *97*, 237003. doi:10.1103/PhysRevLett.97.237003.
18. Chen, W.; Shen, R.; Sheng, L.; Wang, B.G.; Xing, D.Y. Resonant nonlocal Andreev reflection in a narrow quantum spin Hall system. *Physical Review B* **2011**, *84*, 115420. doi:10.1103/PhysRevB.84.115420.
19. Liu, J.; Song, J.; Sun, Q.f.; Xie, X.C. Even-odd interference effect in a topological superconducting wire. *Physical Review B* **2017**, *96*, 195307. doi:10.1103/PhysRevB.96.195307.
20. Reeg, C.; Klinovaja, J.; Loss, D. Destructive interference of direct and crossed Andreev pairing in a system of two nanowires coupled via an s -wave superconductor. *Physical Review B* **2017**, *96*, 081301. doi:10.1103/PhysRevB.96.081301.
21. Zhang, K.; Zeng, J.; Dong, X.; Cheng, Q. Spin dependence of crossed Andreev reflection and electron tunneling induced by Majorana fermions. *Journal of Physics: Condensed Matter* **2018**, *30*, 505302. doi:10.1088/1361-648X/aaedf6.
22. Liu, Y.; Yu, Z.M.; Liu, J.; Jiang, H.; Yang, S.A. Transverse shift in crossed Andreev reflection. *Physical Review B* **2018**, *98*, 195141. doi:10.1103/PhysRevB.98.195141.
23. Wang, Y.X.; Wang, X.; Li, Y.X. Double local and double nonlocal Andreev reflections in nodal-line semimetal-superconducting heterostructures. *Physical Review B* **2022**, *105*, 195402. doi:10.1103/PhysRevB.105.195402.
24. Galambos, T.H.; Ronetti, F.; Hetényi, B.; Loss, D.; Klinovaja, J. Crossed Andreev reflection in spin-polarized chiral edge states due to the Meissner effect. *Physical Review B* **2022**, *106*, 075410. doi:10.1103/PhysRevB.106.075410.
25. Gül, Ö.; Ronen, Y.; Lee, S.Y.; Shapourian, H.; Zauberman, J.; Lee, Y.H.; Watanabe, K.; Taniguchi, T.; Vishwanath, A.; Yacoby, A.; Kim, P. Andreev Reflection in the Fractional Quantum Hall State. *Physical Review X* **2022**, *12*, 021057. doi:10.1103/PhysRevX.12.021057.
26. Reinthaler, R.W.; Recher, P.; Hankiewicz, E.M. Proposal for an all-electrical detection of crossed Andreev reflection in topological insulators. *Physical review letters* **2013**, *110*, 226802. doi:10.1103/PhysRevLett.110.226802.
27. Wang, J.; Hao, L.; Chan, K.S. Quantized crossed-Andreev reflection in spin-valley topological insulators. *Physical Review B* **2015**, *91*, 085415. doi:10.1103/PhysRevB.91.085415.
28. Zhang, Y.T.; Hou, Z.; Xie, X.C.; Sun, Q.f. Quantum perfect crossed Andreev reflection in top-gated quantum anomalous Hall insulator–superconductor junctions. *Physical Review B* **2017**, *95*, 245433. doi:10.1103/PhysRevB.95.245433.
29. Zhou, Y.F.; Hou, Z.; Zhang, Y.T.; Sun, Q.f. Chiral Majorana fermion modes regulated by a scanning tunneling microscope tip. *Physical Review B* **2018**, *97*, 115452. doi:10.1103/PhysRevB.97.115452.
30. Zhang, S.B.; Trauzettel, B. Perfect Crossed Andreev Reflection in Dirac Hybrid Junctions in the Quantum Hall Regime. *Physical review letters* **2019**, *122*, 257701. doi:10.1103/PhysRevLett.122.257701.
31. Li, Q.; Han, Y.; Zhang, K.; Zhang, Y.T.; Liu, J.J.; Qiao, Z. Multiple Majorana edge modes in magnetic topological insulator–superconductor heterostructures. *Physical Review B* **2020**, *102*, 205402. doi:10.1103/PhysRevB.102.205402.

32. Jakobsen, M.F.; Brataas, A.; Qaiumzadeh, A. Electrically Controlled Crossed Andreev Reflection in Two-Dimensional Antiferromagnets. *Physical Review Letters* **2021**, *127*, 017701. doi:10.1103/PhysRevLett.127.017701.
33. Lu, W.T.; Sun, Q.f. Electrical control of crossed Andreev reflection and spin-valley switch in antiferromagnet/superconductor junctions. *Physical Review B* **2021**, *104*, 045418. doi:10.1103/PhysRevB.104.045418.
34. Fuchs, J.; Barth, M.; Gorini, C.; Adagideli, İ.; Richter, K. Crossed Andreev reflection in topological insulator nanowire T junctions. *Physical Review B* **2021**, *104*, 085415. doi:10.1103/PhysRevB.104.085415.
35. Cayssol, J. Crossed Andreev Reflection in a Graphene Bipolar Transistor. *Physical Review Letters* **2008**, *100*, 147001. doi:10.1103/PhysRevLett.100.147001.
36. Benjamin, C.; Pachos, J.K. Detecting entangled states in graphene via crossed Andreev reflection. *Physical Review B* **2008**, *78*, 235403. doi:10.1103/PhysRevB.78.235403.
37. Wang, J.; Liu, S. Crossed Andreev reflection in a zigzag graphene nanoribbon-superconductor junction. *Physical Review B* **2012**, *85*, 035402. doi:10.1103/PhysRevB.85.035402.
38. Crépin, F.; Hettmansperger, H.; Recher, P.; Trauzettel, B. Even-odd effects in NSN scattering problems: Application to graphene nanoribbons. *Physical Review B* **2013**, *87*, 195440. doi:10.1103/PhysRevB.87.195440.
39. Beconcini, M.; Polini, M.; Taddei, F. Nonlocal superconducting correlations in graphene in the quantum Hall regime. *Physical Review B* **2018**, *97*, 201403. doi:10.1103/PhysRevB.97.201403.
40. Zhao, S.C.; Gao, L.; Cheng, Q.; Sun, Q.f. Perfect crossed Andreev reflection in the proximitized graphene/superconductor/proximitized graphene junctions. *Physical Review B* **2023**, *108*, 134511. doi:10.1103/PhysRevB.108.13
41. Xiao-Ling, L.; Zhe, L.; Hai-Bo, Y.; Li-Wei, J.; Wen-Zhu, G.; Yi-Song, Z. Valley polarized electronic transmission through a line defect superlattice of graphene. *Physical Review B* **2012**, *86*, 045410. doi:10.1103/PhysRevB.86.045410.
42. Zihlmann, S.; Cummings, A.W.; Garcia, J.H.; Kedves, M.; Watanabe, K.; Taniguchi, T.; Schönenberger, C.; Makk, P. Large spin relaxation anisotropy and valley-Zeeman spin-orbit coupling in WSe2 /graphene/ h-BN heterostructures. *Physical Review B* **2018**, *97*, 075434. doi:10.1103/PhysRevB.97.075434.
43. Zollner, K.; Fabian, J. Proximity effects in graphene on monolayers of transition-metal phosphorus trichalcogenides MPX3(M:Mn, Fe, Ni, Co, and X: S, Se). *Physical Review B* **2022**, *106*, 035137. doi:10.1103/PhysRevB.106.035137.
44. Khatibi, Z.; Power, S.R. Proximity spin-orbit coupling in graphene on alloyed transition metal dichalcogenides. *Physical Review B* **2022**, *106*, 125417. doi:10.1103/PhysRevB.106.125417.
45. Zollner, K.; Cummings, A.W.; Roche, S.; Fabian, J. Graphene on two-dimensional hexagonal BN, AlN, and GaN: Electronic, spin-orbit, and spin relaxation properties. *Physical Review B* **2021**, *103*, 075129. doi:10.1103/PhysRevB.103.075129.
46. Wakamura, T.; Reale, F.; Palczynski, P.; Zhao, M.Q.; Johnson, A.T.C.; Guéron, S.; Mattevi, C.; Ouerghi, A.; Bouchiat, H. Spin-orbit interaction induced in graphene by transition metal dichalcogenides. *Physical Review B* **2019**, *99*, 245402. doi:10.1103/PhysRevB.99.245402.
47. Frank, T.; Gmitra, M.; Fabian, J. Theory of electronic and spin-orbit proximity effects in graphene on Cu(111). *Physical Review B* **2016**, *93*, 155142. doi:10.1103/PhysRevB.93.155142.
48. Waintal, X.; Wimmer, M.; Akhmerov, A.; Groth, C.; Nikolic, B.K.; Istas, M.; Rosdahl, T.Ö.; Varjas, D. Computational quantum transport. doi:10.48550/arXiv.2407.16257.
49. Groth, C.W.; Wimmer, M.; Akhmerov, A.R.; Waintal, X. Kwant: a software package for quantum transport. *New Journal of Physics* **2014**, *16*, 063065. doi:10.1088/1367-2630/16/6/063065.
50. Jana, K.; Muralidharan, B. Robust all-electrical topological valley filtering using monolayer 2D-Xenes. *npj 2D Materials and Applications* **2022**, *6*, 19. doi:10.1038/s41699-022-00291-y.
51. Blonder, G.E.; Tinkham, M.; Klapwijk, T.M. Transition from metallic to tunneling regimes in superconducting microconstrictions: Excess current, charge imbalance, and supercurrent conversion. *Physical Review B* **1982**, *25*, 4515–4532. doi:10.1103/PhysRevB.25.4515.
52. Liu, Y.; Song, J.; Li, Y.; Liu, Y.; Sun, Q.f. Controllable valley polarization using graphene multiple topological line defects. *Physical Review B* **2013**, *87*, 195445. doi:10.1103/PhysRevB.87.195445.